Results in Physics 59 (2024) 107590

Contents lists available at ScienceDirect

Results in Physics

journal homepage: www.elsevier.com/locate/rinp

Hydrogen diffusion in BCC-Fe: DFT study of tensorial stress effects and interactions with point defects

Gonzalo Álvarez [a], Javier Sánchez [b], Javier Segurado [a,c], Pedro L. de Andres [d], Álvaro Ridruejo [a,*]

[a] Universidad Politécnica de Madrid, Department of Materials Science, E.T.S.I. Caminos, C/ Profesor Aranguren 3, 28040, Madrid, Spain
[b] Instituto de Ciencias de la Construcción Eduardo Torroja-CSIC, C/ Serrano Galvache 4, 28033, Madrid, Spain
[c] IMDEA Materials Institute, Calle Eric Kandel 2, 28906, Getafe, Spain
[d] Instituto de Ciencia de Materiales de Madrid-CSIC, C/ Sor Juana Inés de la Cruz 3, 28049, Madrid, Spain

ARTICLE INFO

Dataset link: https://doi.org/10.21950/CW20RU

Keywords:
BCC-Fe
DFT
Hydrogen diffusion
Defect characterization
Hydrogen embrittlement
Tensorial stress

ABSTRACT

Hydrogen embrittlement is a multifaceted phenomenon that can significantly compromise the toughness of susceptible metals. We study the critical process of hydrogen diffusion within the body-centered cubic lattice of iron (BCC-Fe or α−Fe) using ab-initio density functional theory (DFT). Beyond standard investigations on the effect of hydrostatic stress, we extend our study to incorporate the influence of uniaxial and pure shear stress states. We find substantial alterations in diffusion barriers. Moreover, we study scenarios involving paired point (zero-dimensional) defects, including one vacancy and an additional interstitial hydrogen atom. Calculations comprehend various configurations and transitions between them, providing insight into the interplay between the chemical environment and mechanical fields. The barrier values here determined offer essential data for complementary techniques, including Monte-Carlo models, to accurately describe hydrogen diffusion. This research contributes to a deeper understanding of hydrogen embrittlement, offering insight that can inform the design of safer materials used in structural engineering.

Introduction

Low-alloy (including low-carbon) steels are the most used metallic material in structural components, particularly for applications in which a combination of high toughness and good weldability is required. Among the degradation phenomena that affect them, those leading to the catastrophic failure of structural components, such as hydrogen embrittlement (HE), deserve particular attention due to the associated hazards to human lives [1].

Currently, five different models describing HE are considered: Hydrogen-Enhanced Decohesion (HEDE) [2,3], Hydrogen-Enhanced Localized Plasticity (HELP) [4,5], HELP-mediated HEDE [6], HELP + HEDE [6,7] and Hydrogen-Induced Phase Transformation (HIPT) [8,9].

The differences between these models are related to the strength and interplay of the embrittlement mechanisms that have been proposed. The first of them is HID (Hydrogen-Induced Decohesion), in which embrittlement is explained as a consequence of local reduction in cohesive energy [10–12]. This mechanism is often undistinguished from the HEDE model in the literature, as the HEDE model is based on the effect of the HID mechanism alone. The LHEDM (Local Hydrogen Enhancement of Dislocation Motion) mechanism relates embrittlement to a local decrease of either Peierls stress or the drag forces of dislocations [12–15]. The LHEDM mechanism is often undistinguished from the HELP model in the literature. However, the LHEDM mechanism is only one of the different mechanisms considered by the HELP model, together with AIDE, HESIV, and DC. AIDE (Adsorption-Induced Dislocation Emission) links embrittlement to the increased emission of dislocations from surfaces in which hydrogen has been adsorbed [16,17], while HESIV (Hydrogen-Enhanced, Stress-Induced Vacancy formation), connects embrittlement to the superabundant formation of vacancies in the presence of hydrogen [18,19]. According to the DC (Defactant Concept) mechanism, embrittlement is a consequence of the increased thermodynamical stability of different lattice defects in the presence of hydrogen [20]. HIFF (Hydrogen-Induced Fast Fracture), suggests that embrittlement is the consequence of a two-step process involving the local reduction of plasticity due to the presence of hydrogen around a cavity followed by crack propagation with lower hydrogen content from sharp defects [21,22]. Lastly, the HIPT mechanism coincides with the homonym model and attributes embrittlement to phase transformation [23].

* Corresponding author.
E-mail addresses: g.alvarezm@upm.es (G. Álvarez), javier.sanchez@csic.es (J. Sánchez), javier.segurado@upm.es (J. Segurado), pedro.deandres@csic.es (P.L. de Andres), alvaro.ridruejo@upm.es (Á. Ridruejo).

https://doi.org/10.1016/j.rinp.2024.107590
Received 15 December 2023; Received in revised form 19 February 2024; Accepted 18 March 2024
Available online 19 March 2024

It must be noticed that the relative strength of the different HE mechanisms is highly dependent on the metallic alloy, the local stress state, temperature, the local defect concentration and the balance between strain rate and hydrogen mobility both in bulk and traps. Therefore, we focus on the relevant conditions for structural failure, e.g. interstitial hydrogen on BCC-iron (the stable allotropic state at room temperature) under different applied stresses, aiming to understand the effect of shear stresses for the first time.

HE is a multiscale problem in which hydrogen diffusion is influenced by mechanisms occurring at various scales, ranging from the nanoscale to the micro-, meso- and macroscale, each of them with significantly different characteristic times. The interplay between the different scales is far from straightforward. To comprehend such intricate phenomena, researchers have employed techniques such as ab-initio methods [24–37], molecular statics (MS) [38,39] and molecular dynamics (MD) [40–43]. Thus, simplified models have served as a foundation for developing more complex and realistic approaches in subsequent research [41,42,44]

In order to understand the different aspects of the diffusion of hydrogen, it is important to characterize both its preferential sites and the possible diffusion paths. This can be performed by analyzing the changes on the energy of the system associated to the insertion of an interstitial atom, by evaluating the minimum energy configuration after placing the interstitial atom on the relevant positions of the host lattice, and by observing how the energy is altered under different conditions. Density functional theory (DFT) suits perfectly this kind of calculation and has the advantage that it does not lead to biased results caused by *ad hoc* assumptions.

Prior studies [24–37] based on DFT calculations have reported stationary lattice sites and transition barriers under stress-free and hydrostatic conditions. Additionally, these studies examined interactions between interstitial hydrogen and point defects located in the closest spatial configurations for each interaction. However, they have overlooked the description of other significant configurations relevant to these interactions. In this regard, this work goes beyond these studies by characterizing the preferential interstitial sites and diffusion paths affected by external stresses and defects, with the aim of expanding current knowledge beyond first-order approximations.

Such characterization is divided into three different parts. First, we present the energy landscape without external stress, giving a description of the system and its diffusion paths. Second, we systematically explore the effect of external stress, a tensorial physical magnitude previously reduced to a single scalar value (hydrostatic approximation) on hydrogen diffusion barriers. Hydrostatic, uniaxial and shear stress states are considered. In particular, we find that shear stress plays a significant yet consistently overlooked role. Its analysis is complex, as it depends on the lattice site and its orientation. For instance, shear stress can double hydrogen mobility even for moderate stress levels, significantly modifying the accepted scenario. In the final part of the study, the influence of complex interactions with common point defects in the BCC-iron lattice (either a vacancy or a second interstitial hydrogen) are taken into account up to a distance of 5 Å.

Ab initio characterization methodology

Spin-polarized DFT calculations with a plane-wave basis set [45–48] using the Cambridge Serial Total Energy Package (CASTEP) [49] have been performed. The exchange and correlation energy has been computed within the Perdew–Burke–Ernzerhof generalized-gradient approximation (PBE) [48]. The calculations employed non-linear core-corrected ultrasoft pseudopotentials and relativistic corrections were incorporated for increased accuracy and performance [50,51]. Electronic minimization was done with a density mixing algorithm following the Pulay scheme [52] over a 30-step history. A Gaussian scheme is used for energy level smearing with a width of 0.1 eV [53–55]. Convergence tolerance for energy minimization of 10^{-5} eV/atom and an energy cutoff value for the basis set of 375 eV with a finite basis set correction based on three points differing on 5 eV were used for all calculations. *k*-point sampling of 6 × 6 × 6 and 4 × 4 × 4 was performed for 2 × 2 × 2 and 3 × 3 × 3 supercells, respectively, using the Monkhorst–Pack grid arrangement [56], which correspond to convergence tests of about 2% or better in the optimization of the corresponding unit cell parameter for the pristine material. Finally, geometry optimizations were obtained with the Broyden–Fletcher–Goldfarb–Shanno (BFGS) method [57] until forces on each atom were reduced to values under 10 meV/Å. Zero point energy (ZPE) corrections were performed by evaluation of the Helmholtz free energy at T = 0 K [37] from the calculated phonon spectra (see Section "Phonon spectra", Fig. C.1) [58].

α-Fe calculations

To assess the suitability and benchmark the selected pseudopotentials, energy cutoff, number of special points, and other parameters relevant for the calculation, we examine a few characteristic physical parameters on 2 × 2 × 2 and 3 × 3 × 3 *α*-Fe supercells, denoted as Fe_{16} and Fe_{54}.

α-Fe + H

2 × 2 × 2 and 3 × 3 × 3 *α*-Fe supercells, including one interstitial hydrogen ($Fe_{16}H$ and $Fe_{54}H$), have been used for calculating hydrogen energy landscapes on a BCC-Fe lattice. In the $Fe_{16}H$ supercell, a complete energy landscape has been generated with a spatial resolution of a twentieth of the lattice parameter. The interstitial hydrogen has been placed on a regular grid, allowing full ionic and lattice relaxation.

The geometry optimization of high symmetry sites, namely tetrahedral (T), octahedral (O) and the first-degree saddle point between tetrahedral sites (X), was further refined using the $Fe_{54}H$ cell in a two-step refinement process: First, an initial minimization based on Linear and Quadratic Synchronous Transit (LST/QST) method [59]. Finally, the resulting structures were further refined by minimization under specific symmetry restrictions. The interstitial hydrogen atom occupying high symmetry sites reduces the symmetry of the Fe_{54} cell (space group $Im\bar{3}m$, IT # 229). The space groups of the cells with interstitial hydrogen at site *S* ($Fe_{54}H^S$) are the following: space group $P\bar{4}m2$ (IT # 115) for $Fe_{54}H^T$ (tetragonal site), space group Amm2 (IT # 38) for $Fe_{54}H^X$ (first-degree saddle point) and space group P4/mmm (IT # 123) for $Fe_{54}H^O$ (octahedral site, second-degree saddle point).

Both $Fe_{54}H^T$ and $Fe_{54}H^O$ cells present tetragonal symmetry (a = b ≠ c, $\alpha = \beta = \gamma = 90°$) aligned with one direction from the $\langle 1\,0\,0\rangle$ family of the Fe_{54} cell. The $Fe_{54}H^X$ cell shows orthorhombic symmetry (a ≠,b ≠ c, $\alpha = \beta = \gamma = 90°$), with one of its axis prism primitive cell aligned with a $\langle 0\,0\,1\rangle$ direction of the Fe_{54} cell, and the other two aligned along directions $\langle 1\,1\,0\rangle$ and $\langle 1\,\bar{1}\,0\rangle$.

Note that all the distorted primitive cells ($Fe_{54}H^T$, $Fe_{54}H^O$, and $Fe_{54}H^X$ respectively) show a dissimilar *c* axis, which will be referred to as the **interstitial site orientation** along this work.

The solution energy for hydrogen placed at a generic point P, E_P^{Sol} can be calculated as

$$E_P^{Sol} = E_{Fe_{54}H^P} - E_{Fe_{54}} - \frac{1}{2}E_{H_2}, \tag{1}$$

where E_{H_2} is the energy of a H_2 molecule in vacuum.

Diffusion paths

The diffusion paths reported in the literature are essentially reduced to combinations of elementary transitions between tetrahedral sites, either through the first-degree saddle point, T→X→T, or through the second degree saddle point (octahedral site), T→O→T [11,29,33,37].

When considering such diffusion paths for a net displacement of one lattice parameter along the direction in the $\langle 1\,0\,0\rangle$ family (Fig. 1) , several alternative paths become distinguishable. In this analysis, we

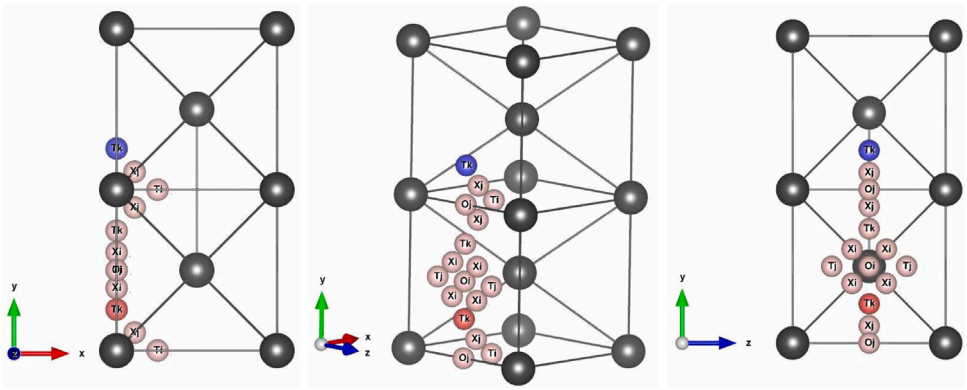

Fig. 1. T, X & O sites involved in a transition along one unit cell from an initial T site (red) to its translationally symmetric site (blue). (For interpretation of the references to color in this figure legend, the reader is referred to the web version of this article.)

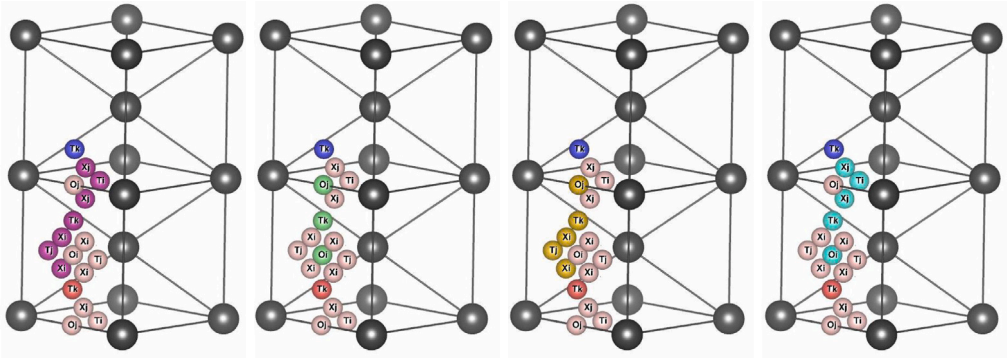

Fig. 2. Absolutely monotonically advancing trajectories for a total displacement of one atomic cell along $\vec{k}$ direction. High symmetry sites are labeled by their type (T, O, X) and site alignment direction (i, j, k). (a) X path. (b) O path. (c) XO path. (d) OX path.

thoroughly examine these pathways. Among these alternatives, only four trajectories consist solely of steps with a positive net advancement, which for the sake of notation clarity, we label as *absolutely monotonically advancing trajectories* (Fig. 2). These trajectories are as follows: (i) The trajectory through the first-degree saddle points (X path), T→X→T→X→T→X→T→X→T, (Fig. 2(a)) (ii) the pure octahedral trajectory (O path), T→O→T→O→T and (Fig. 2(b)), two mixed trajectories (XO path), T→X→T→X→T→O→T (Fig. 2(c)) and (OX path), (T→O→T→X→T→X→T), (Fig. 2(d)) which consist of pair combinations of halves of pure trajectories.

Diffusion paths in Fig. 2 show four different T→X→T transitions, $T_k \to X_j \to T_i$, $T_i \to X_j \to T_k$, $T_k \to X_i \to T_j$ and, $T_j \to X_i \to T_k$ and two T→O→T transitions, $T_k \to O_j \to T_k$ and, $T_k \to O_i \to T_k$.

From these paths the following observations can be made: (i) In a T→X→T transition, each site is oriented along one of the three directions in the $\langle 1\,0\,0 \rangle$ family. (ii) In a T→O→T transition, both T sites are oriented along the same $\langle 1\,0\,0 \rangle$ direction, while the O site is oriented along one of the remaining two directions. (iii) T sites are never oriented towards the same direction as the saddle points surrounding it.

These observations allow the reduction of the number of studied transitions to those starting from a tetrahedral site (T) with any orientation and jumping through either a first (X) or second degree (O) saddle point oriented perpendicularly to the tetrahedral site. The transition ends in a tetrahedral site oriented according to the previous observations (i) & (ii), i.e. $T_1 \to X_2 \to T_3$, $T_1 \to O_2 \to T_1$

Influence of external stress

We have performed calculations to determine the impact of an external homogeneous stress field on energy barriers. These calculations involved relaxing the cell under the influence of the external stress field, with an interstitial hydrogen atom placed in the lattice high symmetry sites (T, X, O). For this study, we considered the following five stress states: (i) hydrostatic (P), (ii) uniaxial stress parallel to the direction aligned with the interstitial defect ($U^{\parallel}$), (iii) uniaxial along one of the directions in $\langle 1\,0\,0 \rangle$ perpendicular to the defect alignment ($U^{\perp}$), (iv) shear in a plane with its normal oriented parallel to the defect alignment ($S^{\parallel}$) and shear in a plane with normal along one of the $\langle 1\,0\,0 \rangle$ directions perpendicular to the defect alignment ($S^{\perp}$). Seven stress levels have been examined: ± 1.8 GPa, ± 0.6 GPa, ± 0.2 GPa and 0 GPa.

Local influence of point defects

Perturbations caused by crystalline defects on the mechanical fields decay slowly away from their core. However, fields in the immediate neighborhood of the defect cannot be represented by quasi-constant values and require detailed calculations for each possible scenario. To study these cases, configurations where a hydrogen atom is found near another hydrogen atom or near a vacancy have been computed. Since hydrogen atoms are light and diffuse relatively quickly, the iron lattice

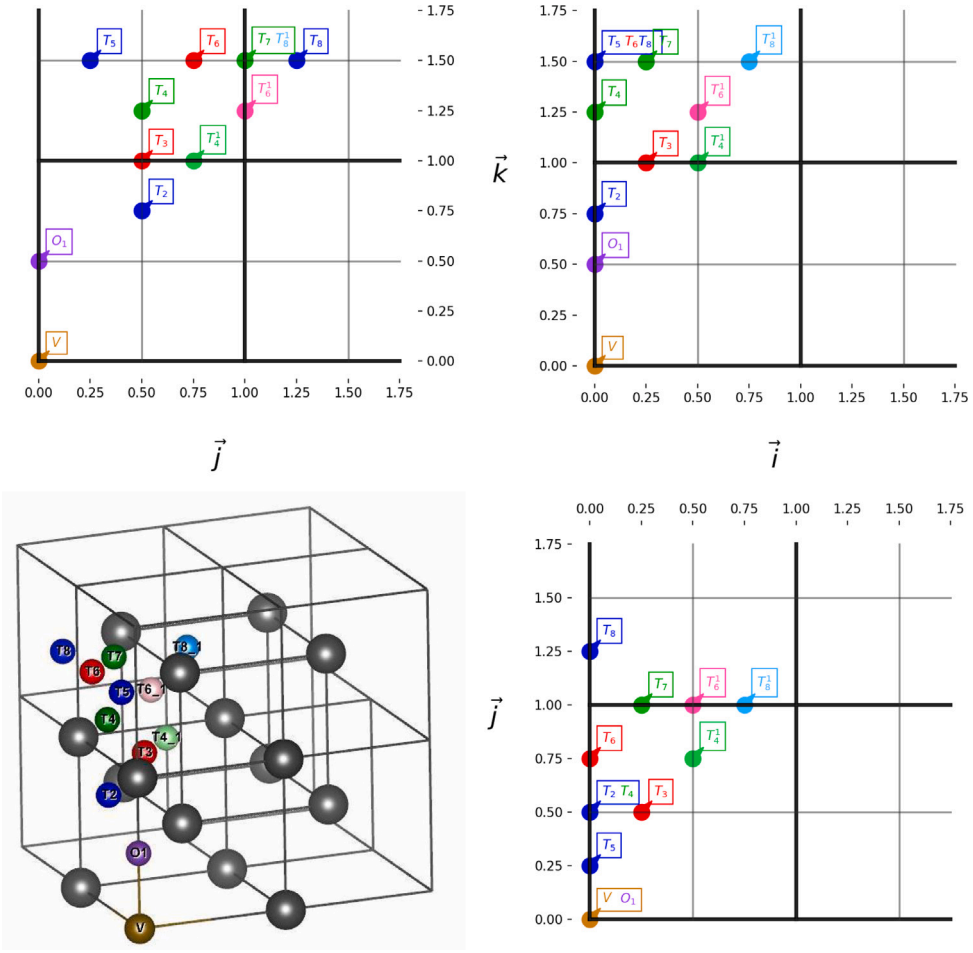

Fig. 3. Relative position of the different configurations in a $Fe_{53}H$ calculation. The vacancy is always located at the origin.

lacks the time required to react to changes in the interstitial position and, consequently, modify the volume of the unit cell containing the interstitial. Additionally, this volume is constrained by the surrounding pristine material's pressure. Therefore, we adopt the simplification of keeping a fixed unit cell volume throughout the diffusion process.

To this end, the minimum energy configuration for each set of calculations, *α-Fe + H + vacancy and α-Fe + H + H*, have been optimized, and the resulting cell dimensions have been fixed.

α-Fe + H + vacancy

The lattice distortion caused by a single iron vacancy is large enough to require a minimum supercell size of 3 × 3 × 3 for simulations involving both one vacancy and one hydrogen atom ($Fe_{53}H$). Calculations were performed for all configurations in which the interstitial hydrogen was placed inside a box aligned with the crystal directions and centered in the vacancy. This box had dimensions 1.5×1.5×1.5 times the BCC-Fe lattice parameter. Such a region encompasses all the local minima on the hydrogen energy landscape, including the neighboring tetrahedral sites, the nearest octahedral site, and the hydrogen located near the vacancy site (Fig. 3). It also includes the allowed transitions between these sites to capture diffusion barriers. The binding energy between the interstitial hydrogen and the vacancy is obtained from the following expression [33]:

$$E^{Bind}_{H-Vac} = -E_{Fe_{53}H} + E_{Fe_{54}H} + E_{Fe_{53}} - E_{Fe_{54}} \quad (2)$$

α-Fe + H + H

We performed a simulation to study the interaction between two hydrogen atoms in a 3 × 3 × 3 Fe supercell that contains two hydrogen interstitials ($Fe_{54}H_2$). The interaction between hydrogen atoms was determined by evaluating the binding energy E^{Bind}_{HH} (Eq. (3)) for various configurations in which one hydrogen was placed inside a box with sides equal to the BCC-Fe lattice parameter and aligned with the crystal directions, centered around the other hydrogen. Lastly, we have also considered all allowed transitions between these configurations (Fig. 4).

$$E^{Bind}_{HH} = -E_{Fe_{54}HH} + 2\,E_{Fe_{54}HT} - E_{Fe_{54}} \quad (3)$$

Results

α-Fe calculations

The Fe_{54} cell converged after relaxation to cell parameters $a = b = c = 8.439$ Å and $\alpha = \beta = \gamma = 90°$, which corresponds to a single cell lattice parameter of 2.813 Å. Space group $Im\bar{3}m$ (IT # 229). Residual stresses were below 2 MPa ($\sigma_{ii} \leq 2$ MPa $i = x, y, z$). The converged magnetic state was ferromagnetic, with a magnetic moment per iron atom of 2.2 μ_B. These quantities show errors $\leq 2\%$ compared to the established experimental values of 2.867 Å and 2.22 μ_B [60], establishing the adequacy of the various parameters in the model.

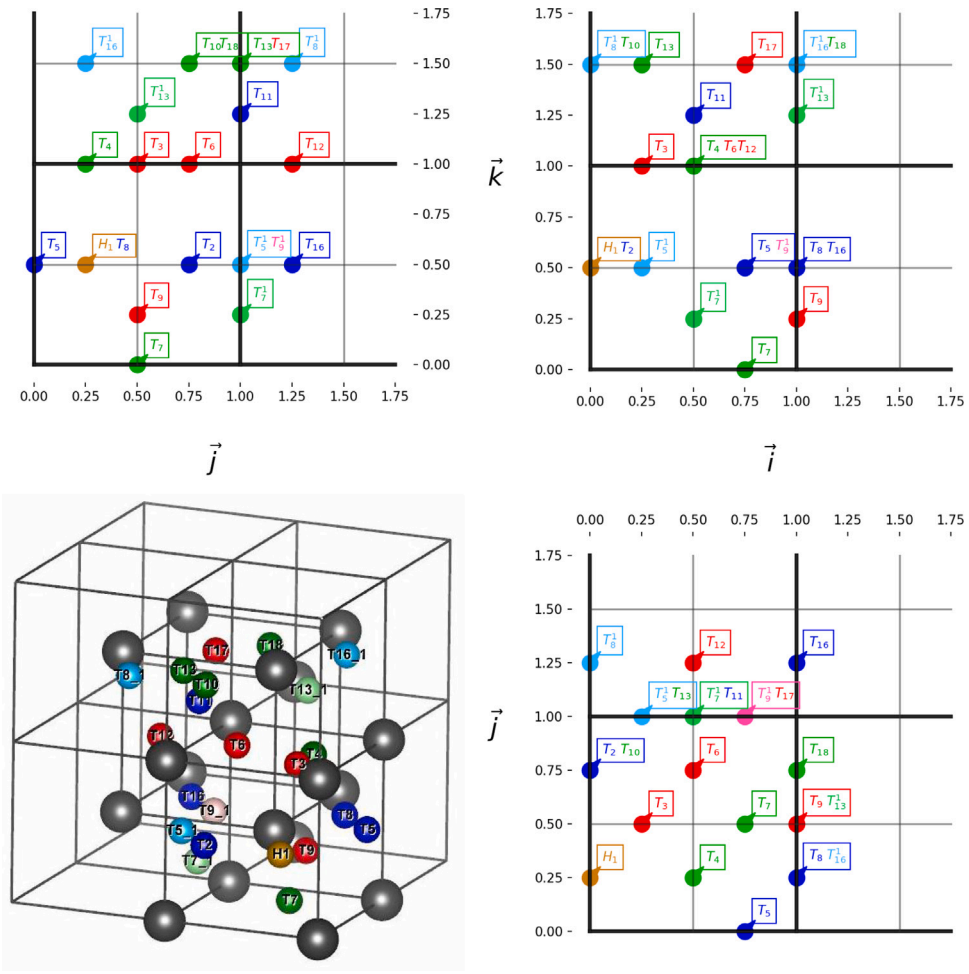

Fig. 4. Relative position of the different configurations in a $Fe_{54}H_2$ calculation.

α-Fe + H

To facilitate a direct comparison with results published in the literature [29,30,33,35–37], we revisit the case of a single hydrogen interstitial inside the BCC-Fe matrix. First, we employed a small simulation cell, $Fe_{16}H$, which proved sufficient to accurately reproduce the basic features for the energy landscape for hydrogen in the proximity to both the tetrahedral and octahedral sites of the iron lattice. Here, we did not include other relevant factors that will be explored later. We obtained the normalized energy landscape using a spatial discretization of $\frac{a}{20}$, as displayed in Fig. 5.

As observed in this figure, our simulations confirm three notable points in the BCC-Fe lattice with a single hydrogen as an interstitial: (i) At the considered interstitial's densities, the optimal absorption sites, which correspond to stationary points of minimum energy, are the tetrahedral interstitial sites (T). (ii) The octahedral interstitial sites (O) are second-degree saddle points. (iii) The first-degree saddle points between neighboring tetrahedral sites (X) correspond to the lowest diffusion barriers.

We further investigate these high symmetry sites using the larger $Fe_{54}H$ supercell to simulate a more dilute case. The results of these calculations are summarized as follows:

For the interstitial hydrogen atom occupying the tetrahedral site, labeled as $Fe_{54}H^T$, the cell relaxed to a = b = 8.461 Å, c = 8.448 Å and $\alpha = \beta = \gamma = 90°$ (space group $P\bar{4}m2$, IT # 115). This relaxed cell exhibited small residual stresses $\sigma_{xx} = \sigma_{yy} = -4.2$ MPa and $\sigma_{zz} =$ 3.3 MPa, and a magnetic moment per iron atom of 2.20 μ_B. The solution energy of hydrogen (Eq. (1)) was equal to 173 meV.

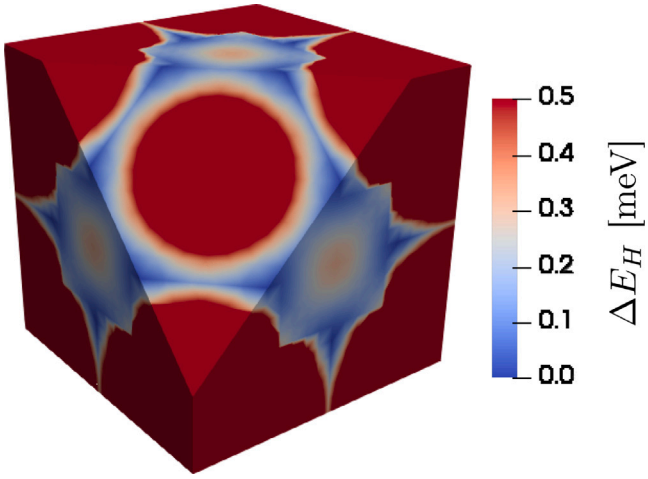

Fig. 5. Hydrogen energy landscape in BCC-Fe cell.

For the X configuration, $Fe_{54}H^X$, in which the hydrogen atom is in the first-degree saddle point, the cell relaxed to a = b = 8.432 Å, c = 8.506 Å, $\alpha = \beta = 90°$ and $\gamma = 89.90°$ (space group Amm2, IT # 38).

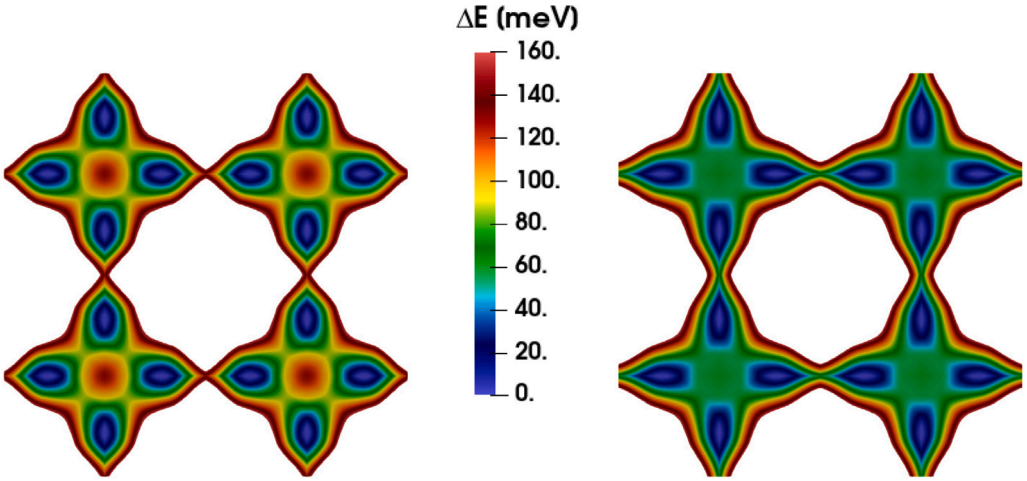

Fig. 6. Effect of ZPE corrections on the hydrogen energy landscape on [0 0 1] plane of $Fe_{54}H$. (a) Configuration without ZPE corrections. (b) ZPE-corrected configuration.

The associated small residual stresses were $\sigma_{xx} = \sigma_{yy} = 2.8$ MPa and $\sigma_{zz} = 2.2$ MPa. The magnetic moment per iron atom was again 2.20 μ_B. As expected, the solution energy of hydrogen (Eq. (1)) increases to 263 meV.

For the configuration with the hydrogen atom in the octahedral site, $Fe_{54}H^O$, the cell parameters relaxed to a = b = 8.420 Å, c = 8.530 Å and $\alpha = \beta = \gamma = 90°$ (space group P4/mmm, IT # 123). Residual stress values were $\sigma_{xx} = \sigma_{yy} = 4.3$ MPa and $\sigma_{zz} = 1.4$ MPa. The magnetic moment per iron atom was again unaffected and kept the value 2.20 μ_B. The solution energy of hydrogen (Eq. (1)) was equal to 301 meV.

The phonon spectra used for the ZPE corrections of the $Fe_{54}H$ cells are provided in Fig. C.1

The diffusion of interstitials modifies the internal stress in the iron matrix, causing it to expand or contract compared to the lattice without hydrogen along the directions parallel, $\epsilon_{\parallel}$, and perpendicular, $\epsilon_{\perp}$, to the interstitial sites orientation by approximately: $\epsilon_{\parallel}^{T} = 0.1\%, \epsilon_{\perp}^{T} = 0.25\%$ in the T-site, $\epsilon_{\parallel}^{O} = 1.1\%, \epsilon_{\perp}^{O} = -0.23\%$ in the O-site, and $\epsilon_{\parallel}^{X} = 0.8\%, \epsilon_{\perp}^{X} = -0.08\%$ in the X-site. Lattice response to these stresses depends on the density and orientation of interstitials and diffusion times, but it is expected to contribute to the elastoplastic behavior of iron and self-consistently modify the diffusion barriers.

Furthermore, we briefly summarize our findings derived from the $Fe_{54}H$ calculations. Tetragonal sites are identified as local minima, whereas octahedral sites are classified as second-degree saddle points. The enthalpy difference between the relaxed configurations is $\Delta E_{T-O} =$ 59 meV per Fe atom. $\Delta E_{T-O}^{NC} = 128$ meV/at, before Zero-Point-Energy corrections (ZPE).

The first-degree saddle point is located near the midpoint between the two nearest tetragonal sites but in a position which slightly deviates from the direct path towards the octahedral site. This first-degree saddle point shows an enthalpy difference of $\Delta E_{T-X} = 56$ meV/at compared to the T site. $\Delta E_{T-X}^{NC} = 90$ meV/at before ZPE correction.

The non-corrected results are in accordance with those of Jiang et al. [29] Hayward et al. [33] and De Andres et al. [37] with values of $\Delta E_{T-O}^{NC} = 120$ meV & $\Delta E_{T-X}^{NC} = 88$ meV, $\Delta E_{T-O}^{NC} = 148$ meV & $\Delta E_{T-X}^{NC} = 90$ meV and $\Delta E_{T-O}^{NC} = 125$ meV & $\Delta E_{T-X}^{NC} = 109$ meV respectively.

Hayward et al. [33] compared the corrected barriers and concluded that both transitions had equivalent barriers, up to the precision of their calculations. A Mulliken analysis of the different configurations shows that the hydrogen atom attracts a small negative charge, −0.33e, −0.032e and −0.31e, when located at T, X and O-sites, respectively, and it carries a negligible amount of spin (−0.05 μ_B,−0.05 μ_B and −0.06 μ_B for T, X and O).

Based on these observations, we infer that the tetragonal (T) site is the only stable point for isolated hydrogen in the absence of defects. The transition between neighboring T sites is easily achieved through the first-degree saddle point (X-site). These pathways compete with transitions via the O-site (a second-degree saddle point). The transition between neighboring T sites is easily achieved either through the first-degree saddle point (X-site) or the competing O-site (a second-degree saddle point).

Due to the difference in the number of constrained directions, and after accounting for ZPE corrections, a negligible difference in enthalpy of $\approx$ 3 meV between the X and O configurations can be observed (Fig. 6). Therefore, both T→X→T and T→O→T transitions, each with corrected energy barriers of $\Delta E_{T-X} = 56$ meV and $\Delta E_{T-O} = 59$ meV, are expected to play a significant role in the diffusion process, as well as near pathways around that region.

Influence of stress states

As mentioned earlier, the stress tensor can influence diffusion paths and barriers, and this aspect has not received a detailed consideration in the literature. Figs. 7, 8, 9 give diffusion barriers between tetrahedral sites for each calculated stress configuration as a function of stress level. Fig. 7 reveals that, contrary to our initial expectations, the effect of hydrostatic stress on the diffusion barriers is almost negligible. However, this is not the case for deviatoric states.

The impact of uniaxial stress states along the ⟨100⟩ directions is shown in Fig. 8. Uniaxial stress states under 2 GPa modify the T→X barrier by as much as 18 meV (20% increase or 32% increase before and after ZPE corrections), effectively doubling or halving the likelihood of the transition to be successful at room temperature.

In contrast, the T→O barrier can be altered up to 10 meV (7.5%) under the same range of uniaxial stresses, resulting in a factor of about 1.5 in the effective transition frequency. It is worth noting that the effect of transitions from a T-site under uniaxial stress applied perpendicularly to the direction aligned with the tetrahedral interstitial defect is similar to the effect of applying stress along the interstitial direction for barriers aligned perpendicularly to the stress, as observed in Fig. 8(b). However, note that the effect is opposite for T and O transition states when stress is applied along the direction aligned with the saddle point defect.

Therefore, tensile uniaxial stress applied in a direction parallel to T sites promotes hydrogen diffusion, particularly favoring T→X transitions. Conversely, compressive stresses marginally increase the

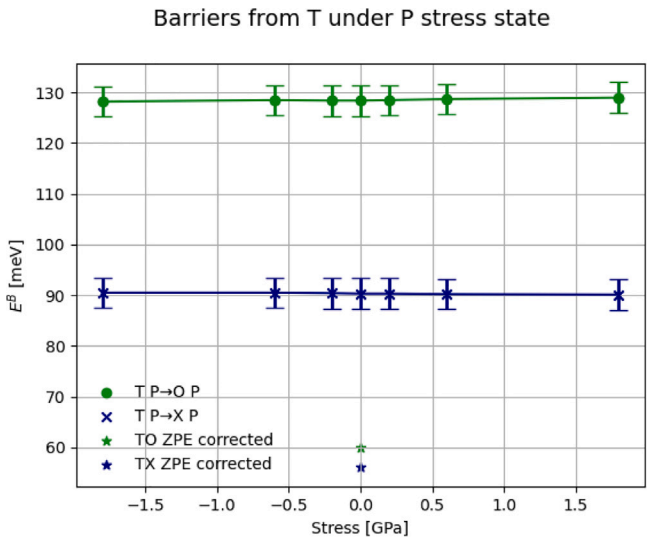

Fig. 7. Diffusion barrier from a tetrahedral site through both X-site (blue) and O-site (green) subjected to hydrostatic stress. (For interpretation of the references to color in this figure legend, the reader is referred to the web version of this article.)

likelihood of T→O transitions, with a minor detriment on a subset of T→X transitions. In conclusion, while the net effect of uniaxial compressive stresses on diffusion can be safely neglected, uniaxial tensile stresses have to be accounted for.

We find the most important effect under shear stress along the {100} planes, Fig. 9. Diffusion barriers are modified differently depending on the relative orientation of the shear plane and the *site orientation*.

When the normal to the shear plane is parallel to the *site orientation* ($S^{\perp}$) Shear stress under 2 GPa decreases the T→X barrier by up to 50 meV (55% and 90% before and after ZPE corrections, respectively), Fig. 9(a). In contrast, the T→O barrier can be reduced by 60 meV (45% and 100% before and after ZPE corrections, respectively) under the same stress range. After applying the ZPE corrections, both resulting barriers become of the order of the accuracy of the calculations (5 ± 5 meV), which Results in almost barrierless diffusion. It is interesting to notice that such an effect is symmetric. The same barrier reduction occurred under positive (tensile) or negative (compressive) stress states.

When the shear plane normal is perpendicular to the tetrahedral *site orientation*, Fig. 9(b), the effect of stress on barriers is quite limited for all transitions, except for the transition to an octahedral site aligned perpendicularly to the applied shear stress plane. In this case, the barrier increases by up to 30 meV at stress levels of 1.8 GPa.

Applied stresses and diffusion paths

Assuming that the material is loaded along the diffusion direction ($\vec{k}$), either uniaxially along the diffusion direction or under shear on a plane perpendicular to the diffusion direction ($\vec{i} \otimes \vec{j}$), the diffusion proceeds along pure trajectories consisting of two equal halves: the X path is composed of two pairs of jumps, each pair consisting of (1) a jump from a T-site aligned parallel to the loading direction to an X-site oriented perpendicular to the loading direction, and (2) of a second jump from a T-site perpendicular to the loading direction to an X-site perpendicular to it, overcoming twice a $TU^{\parallel}\rightarrow XU^{\perp}$ + $TU^{\perp}\rightarrow XU^{\perp}$ pair of barriers. In contrast, the O path must only overcome two equal jumps with $TU^{\parallel}\rightarrow OU^{\perp}$ energy barrier.

On the other hand, loads perpendicular to the diffusion direction make the first and second half of the process different. When considering diffusion along the $\vec{k}$ direction in Fig. 2 while loading along $\vec{j}$ direction, the first half of the X path is a combination of a $TU^{\perp}\rightarrow XU^{\perp}$ jump and a $TU^{\parallel}\rightarrow XU^{\perp}$ jump. In contrast, the second half is made of two $TU^{\perp}\rightarrow XU^{\parallel}$ jumps. Under these conditions, the O path is made of a $TU^{\perp}\rightarrow OU^{\perp}$ and a $TU^{\perp}\rightarrow OU^{\parallel}$ jump. Loading along the $\vec{i}$ direction (instead of along $\vec{j}$) exchanges the half of the transition that occurs first.

We have computed ZPE corrections for each direction and site under stress fields. This evaluation shows variations In the ZPE corrections near the limit of accuracy of our calculation technique ($\left|\Delta ZPE^{Eq}_{i-j} - \Delta ZPE^{\sigma}_{i-j}\right| \leq 4$ meV). The corrected landscapes on $Fe_{54}H$ [0 0 1] plane under uniaxial and shear stresses applied along the (1 0 0) AND (0 0 1) directions can be seen in Fig. 10. When considering the corrected barriers, as shown in Fig. 10(b), it becomes clear that the $TS^{\parallel}\rightarrow XS^{\perp}$ and the $TS^{\parallel}\rightarrow OS^{\perp}$ transitions are significantly reduced to values within the error bars 5 ± 5 meV, resulting in approximately barrierless transitions. However, due to the zigzagging nature of the diffusion path, there is an alternation between barrierless diffusion and diffusion through a barrier similar to the equilibrium $TS^{\perp}\rightarrow XS^{\parallel}$ one. Such an alternation effectively increases the diffusion coefficient by a factor of 2. Note how the existence of regions where the interstitial can diffuse quickly, due to very low barriers, increases the volume accessible to hydrogen.

Although diffusion parallel to the loading direction can be dominated by one of the pure paths or evenly distributed among several pathways depending on the stress state, the landscape for all tetrahedral sites aligned parallel to the stress are the same. A similar scenario happens for the landscape of tetrahedral sites oriented perpendicularly Fig. 10(a) & 10(b).

However, for diffusion path perpendicular to the external stress, i.e., pathways which alternate between a scenario where the saddle points are oriented parallel and perpendicularly to the applied stress, mixed paths are favored, since the stress state promotes different saddle points (O,X) for the parallel and perpendicular orientations Fig. 10(c) & 10(d).

Local influence of point defects

α-Fe + H + vacancy

A single vacancy in the 3 × 3 × 3 Fe supercell (Fe_{53}) constitutes a sufficiently diluted system. Hence, the resulting internal stress is so small that the cubic lattice parameter remains practically unchanged at the value of 8.439 Å (a = 2.813 Å) compared to the supercell for the perfect crystalline system (Fe_{54}), with a relaxation change in the volume $\Omega_0 = -0,093384$ Å^3. The calculated formation enthalpy for the vacancy in our model is 2.51 eV.

The binding energy (E^{Bind}_{H-Vac}, Eq. (2)) between the hydrogen atom and the vacancy for various configurations, along with the distance between the vacancy and hydrogen in the equilibrium configuration, and the angles between the hydrogen-vacancy direction and the different directions in the ⟨1 0 0⟩ family, are given in Table B.1. Values for E^{Bind}_{H-Vac} in Table B.1 show that the first neighboring octahedral site to the vacancy is the most favorable location for hydrogen ($E^{Bind}_{H-Vac} = 733$ meV). In contrast, H in the vacancy site results in an unstable configuration ($E^{Bind}_{H-Vac} = -133$ meV). The other available sites surrounding the vacancy are all stable positions too, with binding energies fluctuating around 65 ± 55 meV, depending on the configuration.

The energy barriers for interstitial hydrogen diffusing between stable configurations are listed in Table 1 (ZPE corrections are not considered here owing to the complexity of computing phonons for such a large cell). hydrogen tends to move close to the vacancy (components below the main diagonal in Table B.1) rather than moving away from it (upper triangular submatrix). Low-energy configurations, such as T_4, have extended residence times.

Rotation of the H-Vacancy complex implies that the diffusion of the hydrogen atom from one octahedral site (O_1) site to another one (O'_1), requires passing through two intermediate sites in a three-step process because the direct transition is forbidden: $O_1 \rightarrow T_2 \rightarrow T'_2 \rightarrow O'_1$, with respective barriers being 651, 67 and 37 meV. Such pathway

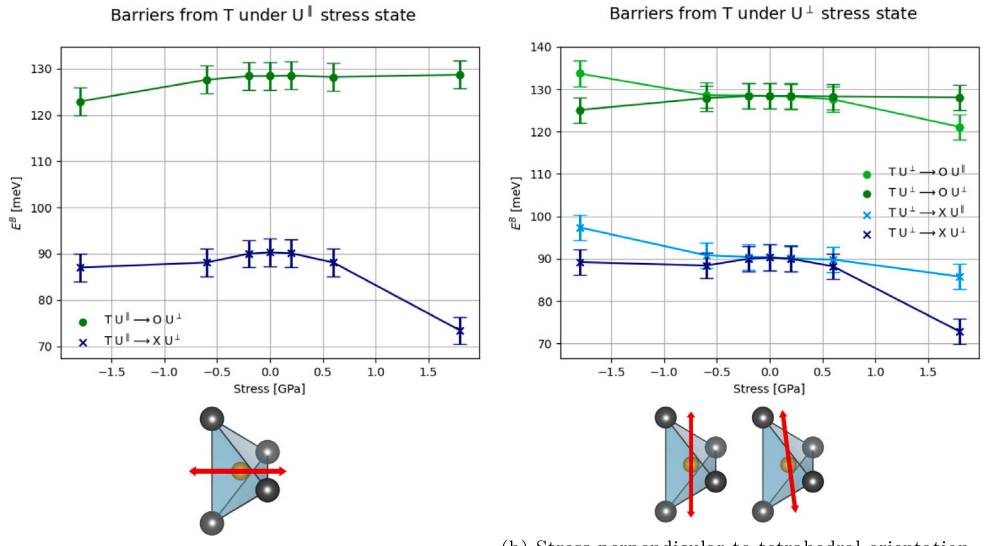

(a) Stress parallel to tetrahedral orientation.

(b) Stress perpendicular to tetrahedral orientation.

Fig. 8. Diffusion barrier from a tetrahedral through both X-site (blue) and O-site (green) site subjected to uniaxial stress. (For interpretation of the references to color in this figure legend, the reader is referred to the web version of this article.)

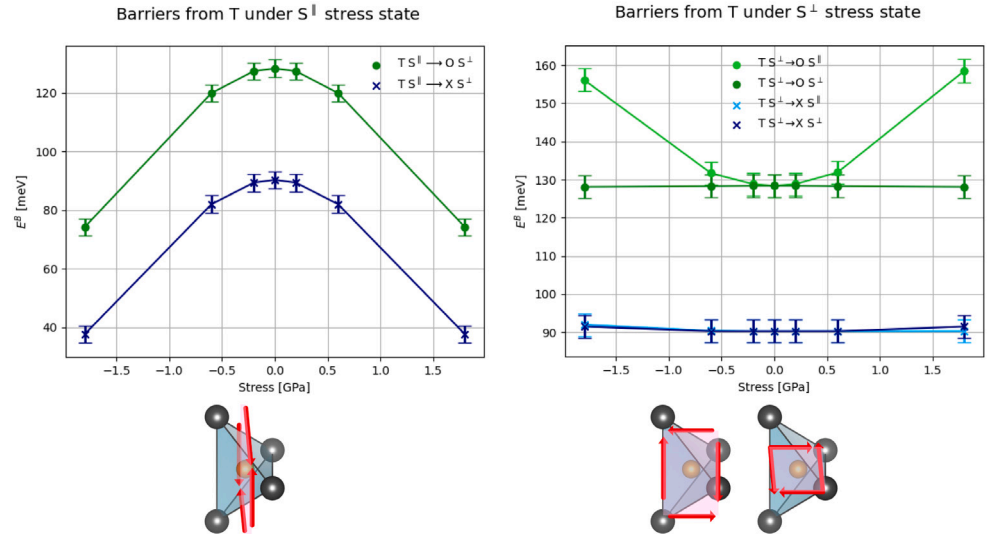

(a) Shear plane with normal parallel to tetrahedral defect orientation.

(b) Shear plane with normal perpendicular to tetrahedral defect orientation.

Fig. 9. Diffusion barriers from a tetrahedral site through both X-site (blue) and O-site (green) subjected to shear stress. (For interpretation of the references to color in this figure legend, the reader is referred to the web version of this article.)

is unlikely due to the large value of the first barrier. We remark that diffusion paths around a vacancy are complex. Therefore, the effective diffusion coefficient around a vacancy requires the individual calculation of various transitions and their associated barriers.

α-Fe + H + H

Since interstitials tend to cluster near vacancies, it is important to study the effect of a second interstitial on diffusion. Such a problem is difficult because its many-body nature and it has been largely ignored in the literature, except for statistical approaches as in [61]. However, the statistical approach lacks specificity of detail. Therefore, here we characterize this problem by listing relevant configurations and by computing the energies involved in the many-body diffusion of two interstitials.

The binding energy (E_{HH}^{Bind}, Eq. (3)) of hydrogen atoms in different configurations and their distances in the bound positions, both in the relaxed and the reference lattice are presented in Table A.1.

As expected, the binding energy between the two hydrogen atoms quickly becomes less negative as their distance increases, being almost negligible for configurations from T_{11} outwards ($d \geq 3.3$ Å). Configurations T_4, T_6 and T_8 show weaker interaction than configurations with similar distances between hydrogen atoms due to the spatial distribution, as these configurations correspond to locations along ⟨1 0 0⟩, ⟨1 1 0⟩

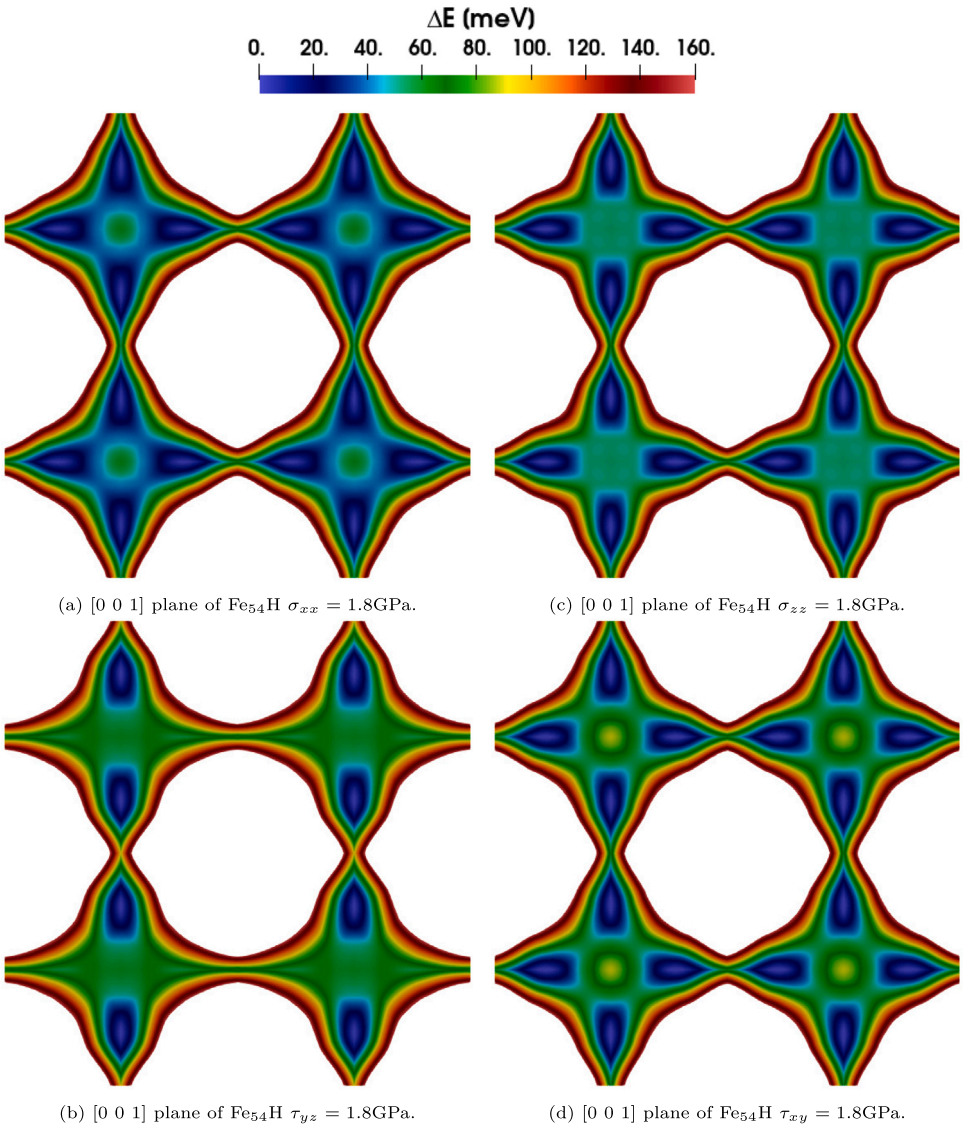

(a) [0 0 1] plane of $Fe_{54}H$ $\sigma_{xx} = 1.8$GPa.

(c) [0 0 1] plane of $Fe_{54}H$ $\sigma_{zz} = 1.8$GPa.

(b) [0 0 1] plane of $Fe_{54}H$ $\tau_{yz} = 1.8$GPa.

(d) [0 0 1] plane of $Fe_{54}H$ $\tau_{xy} = 1.8$GPa.

Fig. 10. Effect of tensile (a,c) and shear (b,d) stress applied along the x (a,b) and z (c,d) directions on the ZPE-corrected hydrogen energy landscape on [0 0 1] plane of $Fe_{54}H$.

Table 1
Energy barrier of transitions from position in row to position in column, $\Delta E_{r\to c}$ in a $Fe_{53}H$ cell.

$\Delta E_{r\to c}$ meV	O_1	T_2	T_3	T_4	T_4^1	T_5	T_6	T_6^1	T_7	T_8	T_8^1
O_1		651									
T_2	37	67	123								
T_3		64	49	21	108						
T_4			68	31							
T_4^1			79			85	72				
T_5					40	107					
T_6					80				61		
T_6^1								102	111	115	
T_7							108	114			83
T_8								86		83	
T_8^1									97		124

Table 2
Energy barrier in transitions from position in row to position in column, $\Delta E_{r\to c}$ in a $Fe_{54}HH$ cell.

$\Delta E_{r\to c}$ meV	T_2	T_3	T_4	T_5	T_5^{I}	T_6	T_7	T_7^{I}	T_8	T_8^{I}	T_9	T_9^{I}	T_{10}	T_{11}	T_{12}	T_{13}	T_{13}^{I}	T_{16}	T_{16}^{I}	T_{17}	T_{18}
T_2				11																	
T_3			47		90	56															
T_4		119						112													
T_5	150						116		91												
T_5^{I}		154								90			88								
T_6		124					104	113						100							
T_7				113		96					142				89						
T_7^{I}			101			104						108					89				
T_8				108																	
T_8^{I}					73							158									
T_9							117						100					65			
T_9^{I}								79		142			153								
T_{10}					100						81	138				115					
T_{11}						98									105	108				108	
T_{12}							97							106							
T_{13}													109	111				113			
T_{13}^{I}								99											110		110
T_{16}											97					110					
T_{16}^{I}																	112				
T_{17}														106							108
T_{18}																	108			111	

or ⟨1 1 1⟩ directions, owing to the non-spherical shape of the hydrogen interstitial defect.

The table shows that interactions are less intense when the line connecting the sites is either parallel to a lattice direction or a diagonal both face and body.

Table 2 shows the transition barriers between two configurations with two hydrogen atoms. It is observed that the transition barriers exhibit similar tendencies as the configurations presented in Table A.1, with negligible differences in transitions beyond T_{10} ($\Delta E_{10^{>}\to 10^{>}} = 109 \pm 4$ meV), which indicates the effective range of the interaction.

For configurations near the vacancy, a highly heterogeneous and irregular landscape can be appreciated ($\Delta E_{10^{\leq}\to 10^{\leq}} = 109 \pm 50$ meV). A closer analysis shows that movements to distant configurations (elements in the upper triangular matrix) generally have lower barriers than transitions bringing interstitials closer (elements in the lower triangular matrix) We attribute such a feature to the repulsive nature of the interaction between two interstitial atoms. Transitions to high-energy configurations, such as T_9 & T_9^{I}, display high energy barriers. In contrast, transitions to low-energy configurations exhibit below-average transition barriers.

Transitions from inside the range of the interaction to the outside, ($\Delta E_{10^{\leq}\to 10^{>}}$) and the reverse transitions ($\Delta E_{10^{>}\to 10^{\leq}}$) show the same complex behavior as internal transitions, indicating a sudden smoothing of the interaction core in all directions within this range.

The heterogeneous barriers we have found hint to an energy landscape for a hydrogen atom in the presence of another interstitial hydrogen atom becomes locally complex up to distances of $\approx$ 3.2 Å (T_{10}), beyond which the non-mechanical components of the interaction becomes negligible. Inside those distances of $\approx$ 3.2 Å, the use of individual transition barriers is necessary.

Conclusions

It is generally acknowledged in the literature that hydrogen embrittlement is associated with the accumulation of atomic hydrogen near dislocations or vacancies. Therefore, mechanisms that facilitate the diffusion of interstitials are expected to modify the material sensitivity to this form of structural failure. This concept finds support in experimental observations where hydrogen embrittlement significantly decreases at temperatures exceeding 400–500 K, and original mechanical properties are restored after heat treatment at these temperatures [62,63]. Therefore, our discovery of scenarios where the diffusion barrier diminishes and the interstitial find easy to diffuse to large regions, holds relevance in helping the design of materials resistant to embrittlement.

We have analyzed the effect of non-diagonal stresses on the diffusion barrier of interstitial hydrogen. Unlike the small changes reported previously in the literature for diagonal stresses, we report a large variation in the diffusion barrier for deviatoric states that can modify its value by as much as 100%. Therefore, to obtain accurate values for barriers under shear tension, it is necessary to consider at the same time both the transition involved and the stress state. For instance, a 600 MPa shear stress reduces $TS^{\parallel} \to OS^{\perp}$,$TS^{\parallel} \to XS^{\perp}$ and $TS^{\perp} \to OS^{\parallel}$ barriers by 10 to 15 meV, which increases the success ratio of these transitions by a factor between 1.5 to 2 at room temperature, without any significant effect on the other available transitions. This effect gradually increases up to a stress value of 1.8 GPa, in which the transitions become effectively barrierless, resulting in a diffusion process limited by the greencomplementary transitions (the other half of the trajectory). As a consequence, we find that nontrivial stress-dependent diffusion paths control hydrogen mobility.

We have analyzed in detail the effect of the distortion on the hydrogen local energy landscape near a vacancy and the interaction with a second interstitial hydrogen. We report binding energies for each configuration (within some local range) and the transition barriers among the different configurations. hydrogen-vacancy complexes show interactions that extend over several unit cells, decreasing, as expected, with distance. On the other hand, hydrogen-hydrogen interactions show a shorter range interaction, that can safely be neglected for distances beyond two unit cells. In both cases, the local field is complex, and each specific transition must be considered independently to accurately model hydrogen diffusion in their surroundings.

Therefore, it can be concluded that hydrogen transport in iron, is a complex phenomenon that cannot be described by a global diffusivity constant. Instead, it requires the use of local diffusivity tensors that depend on the crystal orientation, the neighbor defects and the stress state. In this work, we have calculated in some detail the physical effects on the diffusion barriers caused by stresses and point defects, parameters essential to further understand and accurately simulate the processes involved in hydrogen embrittlement.

Table A.1
For each configuration: binding energy, distance between the two hydrogen atoms both in the relaxed configuration (in angstroms) and in the reference configuration (as a fraction of the reference lattice parameter), angles between the H-H direction and the relevant directions in < 100 > family [parallel to the orientation of interstitial H_A and perpendicular directions (angle$_{\perp^1}$ ≤angle$_{\perp^2}$)], and orientation of interstitial H_B.

Configuration	E_{HH}^{Bind} [meV/at]	Distance (relaxed) [Å]	Distance (normalized) [a]	Angle ∥ [°]	Angle $\perp^1$ [°]	Angle $\perp^2$ [°]	Orientation H_A-H_B
T_2	−150	1.924	$\sqrt{2/8}$	0.00	90.00	90.00	∥
T_3	−75	1.859	$\sqrt{3/8}$	64.33	37.78	64.33	$\perp^2$
T_4	−3	2.008	$\sqrt{4/8}$	90.00	45.00	45.00	∥
T_5	−11	2.277	$\sqrt{5/8}$	18.19	71.81	90.00	$\perp^1$
T_5^1	−11	2.276	$\sqrt{5/8}$	71.81	18.19	90.00	$\perp^1$
T_6	−6	2.468	$\sqrt{6/8}$	54.59	54.81	54.81	∥
T_7	−15	2.677	$\sqrt{7/8}$	36.86	57.81	73.99	$\perp^2$
T_7^1	−15	2.677	$\sqrt{7/8}$	74.02	36.86	57.80	$\perp^1$
T_8	6	2.831	$\sqrt{8/8}$	0.00	90.00	90.00	∥
T_8^1	−28	2.859	$\sqrt{8/8}$	90.00	0.00	90.00	∥
T_9	−40	3.116	$\sqrt{9/8}$	45.00	45.00	90.00	$\perp^1$
T_9^1	−44	3.084	$\sqrt{9/8}$	75.26	21.08	75.26	$\perp^2$
T_{10}	−59	3.156	$\sqrt{10/8}$	63.62	26.38	0.00	∥
T_{11}	−8	3.316	$\sqrt{11/8}$	50.28	50.28	64.66	$\perp^1$
T_{12}	−7	3.464	$\sqrt{12/8}$	35.31	65.92	65.83	∥
T_{13}	−5	3.606	$\sqrt{13/8}$	54.03	38.28	78.63	$\perp^2$
T_{13}^1	−5	3.606	$\sqrt{13/8}$	78.63	38.28	54.03	$\perp^2$
T_{16}	−8	4.005	$\sqrt{16/8}$	45.00	45.00	90.00	∥
T_{16}^1	−3	3.999	$\sqrt{16/8}$	90.00	45.00	45.00	∥
T_{17}	−10	4.124	$\sqrt{17/8}$	59.03	46.69	59.03	$\perp^2$
T_{18}	−7	4.245	$\sqrt{18/8}$	70.54	48.21	48.16	∥

Table B.1
For each configuration: binding energy, distance between hydrogen atoms both in the relaxed configuration (in Å) and the reference configuration (as a fraction of the reference lattice parameter) and angles between the vacancy-H direction and the directions in < 100 > family [parallel to the interstitial *site orientation* and along perpendicular directions (angle$_{\perp^1}$ ≤angle$_{\perp^2}$)].

Conf.	E_{H-Vac}^{Bind} [meV/at]	Distance (relaxed) [Å]	Distance (normalized) [a]	Angle ∥ [°]	Angle $\perp^1$ [°]	Angle $\perp^2$ [°]
V	−133	0	0			
O_1	733	1.172	$\sqrt{4}/4$	0.00	90.00	90.00
O_2	56	2.230	$\sqrt{8}/4$	90.00	45.00	45.00
T_2	119	2.542	$\sqrt{13}/4$	33.57	56.43	90.00
T_3	60	3.233	$\sqrt{21}/4$	77.45	29.15	64.15
T_4	107	3.706	$\sqrt{29}/4$	56.90	41.74	67.61
T_4^1	31	3.789	$\sqrt{29}/4$	21.73	68.27	90.00
T_5	14	4.278	$\sqrt{37}/4$	80.46	9.54	90.00
T_6	39	4.718	$\sqrt{45}/4$	63.41	26.59	90.00
T_6^1	83	4.720	$\sqrt{45}/4$	41.83	53.38	72.64
T_7	86	5.122	$\sqrt{53}/4$	82.08	34.54	56.64
T_8	53	5.494	$\sqrt{61}/4$	67.39	39.83	59.18
T_8^1	100	5.495	$\sqrt{61}/4$	50.16	39.84	90.00

CRediT authorship contribution statement

Gonzalo Álvarez: Writing – original draft, Visualization, Software, Methodology, Investigation, Formal analysis, Data curation, Conceptualization. **Javier Sánchez:** Writing – review & editing, Methodology, Conceptualization. **Javier Segurado:** Supervision, Methodology, Conceptualization. **Pedro L. de Andres:** Writing – review & editing, Methodology, Funding acquisition. **Álvaro Ridruejo:** Writing – original draft, Supervision, Project administration, Methodology, Funding acquisition, Conceptualization.

Declaration of competing interest

The authors declare that they have no known competing financial interests or personal relationships that could have appeared to influence the work reported in this paper.

Data availability

Data are stored in the open repository *e-Cienciadatos* and be accessed through the following link: https://doi.org/10.21950/CW20RU.

Acknowledgments

Authors are grateful to the Ministry for Science and Innovation of Spain for the financial support from Grant PID2019-106759GB-I00, funded by MCIN/AEI/10.13039/501100011033.

G. Álvarez is thankful for the scholarship provided by Universidad Politécnica de Madrid and the Ministry for Universities (Ref: FPU20/05495).

P.L. de Andres acknowledges financial support from PID2020-113142RB-C21, funded by MCIN/AEI/10.13039/501100011033 and TED2021-129999B-C31, funded by MCIN/AEI/10.13039/5011000-11033.

Appendix A. Hydrogen-Hydrogen interaction table

See Table A.1.

Appendix B. Hydrogen-vacancy interaction table

See Table B.1.

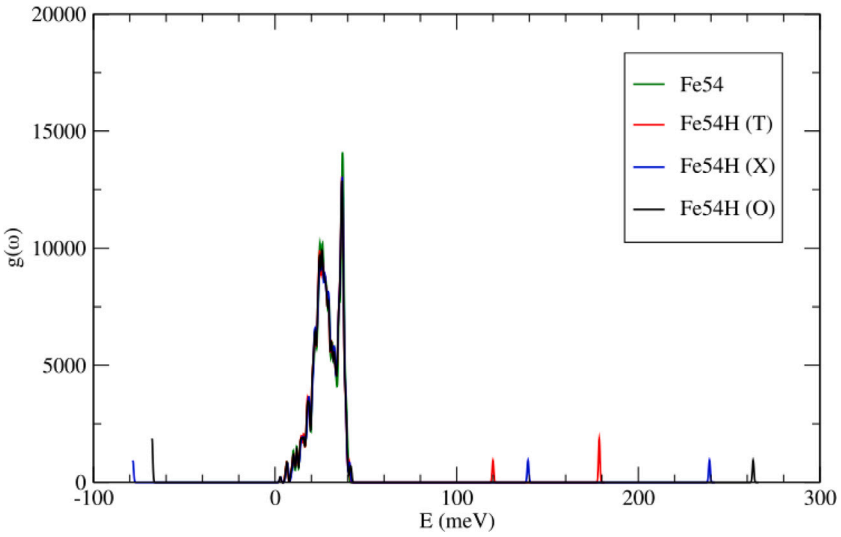

Fig. C.1. Phonon spectra used to compute the zero-point correction in Fe_{54}, $Fe_{54}H^{T}$, $Fe_{54}H^{X}$&$Fe_{54}H^{O}$.

Appendix C. Phonon spectra

See Fig. C.1.

Appendix D. Supplementary data

Supplementary material related to this article can be found online at https://doi.org/10.1016/j.rinp.2024.107590.

References

[1] Sonak S, Tiwari A, Jain U, Keskar N, Kumar S, Singh RN, Dey GK. Effect of pre-strain on susceptibility of Indian reduced activation ferritic martensitic steel to hydrogen embrittlement. J Nucl Mater 2015;465:78–82.
[2] Balan KP. Hydrogen embrittlement and stress corrosion cracking. Metall Failure Anal 2018;179–202.
[3] Dadfarnia M, Nagao A, Wang S, Martin ML, Somerday BP, Sofronis P. Recent advances on hydrogen embrittlement of structural materials. Int J Fract 2015;196(1–2):223–43.
[4] Robertson IM, Sofronis P, Nagao A, Martin ML, Wang S, Gross DW, Nygren KE. Hydrogen embrittlement understood. Metall Mater Trans A: Phys Metall Mater Sci 2015;46(6):2323–41.
[5] Lynch S. Discussion of some recent literature on hydrogen-embrittlement mechanisms: Addressing common misunderstandings. Corros Rev 2019;37(5):377–95.
[6] Djukic MB, Bakic GM, Sijacki Zeravcic V, Sedmak A, Rajicic B. The synergistic action and interplay of hydrogen embrittlement mechanisms in steels and iron: Localized plasticity and decohesion. Eng Fract Mech 2019;216:106528.
[7] Zhao Y, Seok MY, Choi IC, Lee YH, Park SJ, Ramamurty U, Suh JY, Jang JI. The role of hydrogen in hardening/softening steel: Influence of the charging process. Scr Mater 2015;107:46–9.
[8] Motta AT, Chen LQ. Hydride formation in zirconium alloys. Jom 2012;64(12):1403–8.
[9] Billone MC, Burtseva TA, Einziger RE. Ductile-to-brittle transition temperature for high-burnup cladding alloys exposed to simulated drying-storage conditions. J Nucl Mater 2013;433(1–3):431–48.
[10] Turnbull A. Modelling of environment assisted cracking. Corros Sci 1993;34(6):921–60.
[11] Ramasubramaniam A, Itakura M, Carter EA. Interatomic potentials for hydrogen in α -iron based on density functional theory. Phys Rev B - Conden Matter Mater Phys 2009;79(17):174101.
[12] Barrera O, Cocks AC. Computational modelling of hydrogen embrittlement in welded structures. Phil Mag 2013;93(20):2680–700.
[13] Birnbaum HK, Sofronis P. Hydrogen-enhanced localized plasticity-a mechanism for hydrogen-related fracture. Mater Sci Eng A 1994;176(1–2):191–202.
[14] Robertson IM. The effect of hydrogen on dislocation dynamics. Eng Fract Mech 2001;68(6):671–92.
[15] Yu P, Cui Y, zhen Zhu G, Shen Y, Wen M. The key role played by dislocation core radius and energy in hydrogen interaction with dislocations. Acta Mater 2020;185:518–27.
[16] Lynch SP. Comments on "A unified model of environment-assisted cracking". Scr Mater 2009;61(3):331–4.
[17] Lynch SP. Hydrogen embrittlement (HE) phenomena and mechanisms. Stress Corrosion Cracking: Theory Prac 2011;30(3–4):90–130.
[18] Matsuo T, Yamabe J, Matsuoka S. Effects of hydrogen on tensile properties and fracture surface morphologies of type 316L stainless steel. Int J Hydrogen Energy 2014;39(7):3542–51.
[19] Ogosi E, Asim UB, Siddiq A, Kartal ME. Hydrogen effect on plastic deformation and fracture in austenitic stainless steel. In: NACE - international corrosion conference series, vol. 2020-June, OnePetro; 2020.
[20] Kirchheim R. Revisiting hydrogen embrittlement models and hydrogen-induced homogeneous nucleation of dislocations. Scr Mater 2010;62(2):67–70.
[21] Shishvan SS, Csányi G, Deshpande VS. Hydrogen induced fast-fracture. J Mech Phys Solids 2020;134:103740.
[22] Shishvan SS, Csányi G, Deshpande VS. Strain rate sensitivity of the hydrogen embrittlement of ferritic steels. Acta Mater 2023;257:119173.
[23] Pushilina N, Panin A, Syrtanov M, Kashkarov E, Kudiiarov V, Perevalova O, Laptev R, Lider A, Koptyug A. Hydrogen-induced phase transformation and microstructure evolution for Ti-6Al-4V parts produced by electron beam melting. Metals 2018;8(5):301.
[24] Yang LH, Moriarty JA, Wills JM. First-principles formation energies of monovacancies in bcc transition metals. Phys Rev B 1999.
[25] Korzhavyi PA, Ruban AV, Lozovoi AY, Vekilov YK, Abrikosov IA, Johansson B. Constitutional and thermal point defects in *B2* NiAl. Phys Rev B 2000;61:6003.
[26] Domain C, Becquart CS. *Ab initio* calculations of defects in Fe and dilute Fe-Cu alloys. Phys Rev B 2001;65:024103.
[27] Tateyama Y, Ohno T. Stability and clusterization of hydrogen-vacancy complexes in-Fe: An ab initio study. Phys Rev B 2003.
[28] Fu CC, Torre JD, Willaime F, Bocquet JL, Barbu A. Multiscale modelling of defect kinetics in irradiated iron. Nat Mater 2004 4:1 2004;4:68–74.
[29] Jiang DE, Carter EA. Diffusion of interstitial hydrogen into and through bcc Fe from first principles. Phys Rev B - Conden Matter Mater Phys 2004;70(6):064102.
[30] Sanchez J, Fullea J, Andrade C, De Andres PL. Hydrogen in α -iron: Stress and diffusion. Phys Rev B - Conden Matter Mater Phys 2008;78(1):014113.
[31] Nazarov R, Hickel T, Neugebauer J. First-principles study of the thermodynamics of hydrogen-vacancy interaction in fcc iron. Phys Rev B - Conden Matter Mater Phys 2010;82(22):224104.
[32] Counts W, Wolverton C, Gibala R. Binding of multiple h atoms to solute atoms in bcc Fe using first principles. Acta Mater 2011;59(14):5812–20.
[33] Hayward E, Fu CC. Interplay between hydrogen and vacancies in α-Fe. Phys Rev B - Conden Matter Mater Phys 2013;87(17):174103.
[34] Mirzaev DA, Mirzoev AA, Okishev KY, Verkhovykh AV. Hydrogen-vacancy interaction in bcc iron: Ab initio calculations and thermodynamics. Mol Phys 2014;112:1745–54.
[35] He T, Jiang Y, Zhou R, Feng J. Point defect interactions in iron lattice: A first-principles study. RSC Adv 2016;6:45250–8.
[36] He Y, Li Y, Chen C, Yu H. Diffusion coefficient of hydrogen interstitial atom in α-Fe, γ-Fe and ε-Fe crystals by first-principle calculations. Int J Hydrogen Energy 2017;42:27438–45.
[37] de Andres PL, Sanchez J, Ridruejo A. Hydrogen in α-iron: Role of phonons in the diffusion of interstitials at high temperature. Sci Rep 2019;9(1):1–9.
[38] Tewordt L. Distortion of the lattice around an interstitial, a crowdion, and a vacancy in copper. Phys Rev 1958;109(1):61.
[39] Johnson RA. Interstitials and vacancies in alpha-iron. Phys Rev 1964;134(5A):A1329.

[40] Fu CC, Torre JD, Willaime F, Bocquet JL, Barbu A. Multiscale modelling of defect kinetics in irradiated iron. Nat Mater 2005;4(1):68–74.
[41] Hayward E, Beeler B, Deo C. Multiple hydrogen trapping at monovacancies. Phil Mag Lett 2012;92(5):217–25.
[42] Song J, Curtin WA. Atomic mechanism and prediction of hydrogen embrittlement in iron. Nature Mater 2013;12(2):145–51.
[43] Tehranchi A, Curtin WA. The role of atomistic simulations in probing hydrogen effects on plasticity and embrittlement in metals. Eng Fract Mech 2019;216:106502.
[44] Du YA, Rogal J, Drautz R. Diffusion of hydrogen within idealized grains of bcc Fe: A kinetic Monte Carlo study. Phys Rev B - Conden Matter Mater Phys 2012;86(17):174110.
[45] Hans VH. Einführung in die Quantenchemie. Zeitschrift für Elektrochemie und angew physikalische Chemie 1937;44(4):284.
[46] Hohenberg P, Kohn W. Inhomogeneous electron gas. Phys Rev 1964;136:B864–71.
[47] Kohn W, Sham LJ. Self-consistent equations including exchange and correlation effects. Phys Rev 1965;140:A1133–8.
[48] Perdew JP, Burke K, Ernzerhof M. Generalized gradient approximation made simple. Phys Rev Lett 1996;77:3865–8.
[49] Clark SJ, Segall MD, Pickard CJ, Hasnip PJ, Probert MI, Refson K, Payne MC. First principles methods using CASTEP. Zeitschrift fur Kristallographie 2005;220(5–6):567–70.
[50] Koelling DD, Harmon BN. A technique for relativistic spin-polarised calculations. J Phys C: Solid State Phys 1977;10(16):3107.
[51] Louie SG, Froyen S, Cohen ML. Nonlinear ionic pseudopotentials in spin-density-functional calculations. Phys Rev B 1982;26:1738–42.
[52] Rohwedder T, Schneider R, Rohwedder T, Schneider R, Ma S, Schneider R. An analysis for the DIIS acceleration method used in quantum chemistry calculations. J Math Chem 2011;49:1889–914.
[53] Kresse G, Furthmüller J. Efficient iterative schemes for ab initio total-energy calculations using a plane-wave basis set. Phys Rev B 1996;54:11169–86.
[54] Marzari N, Vanderbilt D, Payne MC. Ensemble density-functional theory for Ab initio molecular dynamics of metals and finite-temperature insulators. Phys Rev Lett 1997;79:1337–40.
[55] Mermin ND. Thermal properties of the inhomogeneous electron gas. Phys Rev 1965;137:A1441–3.
[56] Monkhorst HJ, Pack JD. Special points for Brillouin-zone integrations. Phys Rev B 1976;13:5188–92.
[57] Pfrommer BG, Côté M, Louie SG, Cohen ML. Relaxation of crystals with the Quasi-Newton method. J Comput Phys 1997;131(1):233–40.
[58] Refson K, Tulip PR, Clark SJ. Variational density-functional perturbation theory for dielectrics and lattice dynamics. Phys Rev B 2006;73:155114.
[59] Govind N, Petersen M, Fitzgerald G, King-Smith D, Andzelm J. A generalized synchronous transit method for transition state location. Comput Mater Sci 2003;28(2):250–8, Proceedings of the Symposium on Software Development for Process and Materials Design.
[60] Lide DR. CRC handbook of chemistry and physics. CRC Press; 2014.
[61] Sanchez J, Fullea J, Andrade MC, De Andres PL. Ab initio molecular dynamics simulation of hydrogen diffusion in α -iron. Phys Rev B - Conden Matter Mater Phys 2010;81(13):8–11.
[62] Xu K. 14 - Hydrogen embrittlement of carbon steels and their welds. In: Gangloff RP, Somerday BP, editors. Gaseous hydrogen embrittlement of materials in energy technologies. Woodhead publishing series in metals and surface engineering, vol. 2, Woodhead Publishing; 2012, p. 526–61.
[63] Papavinasam S. Chapter 5 - mechanisms. In: Papavinasam S, editor. Corrosion control in the oil and gas industry. Boston: Gulf Professional Publishing; 2014, p. 249–300.